



A flash heating method for measuring thermal conductivity at high pressure and temperature: Application to Pt



R. Stewart McWilliams^{a,b,c}, Zuzana Konôpková^d, Alexander F. Goncharov^{b,e,f,*}

^a School of Physics and Astronomy and Centre for Science at Extreme Conditions, University of Edinburgh, Mayfield Rd., Edinburgh EH9 3FD, UK

^b Geophysical Laboratory, Carnegie Institution of Washington, 5251 Broad Branch Road NW, Washington, DC 20015, USA

^c Departamento de Geociencias, Universidad de Los Andes, Bogotá, Colombia

^d Deutsches Elektronen-Synchrotron (DESY) Photon Science, Notkestraße 85, 22607 Hamburg, Germany

^e Key Laboratory of Materials Physics, Institute of Solid State Physics, Chinese Academy of Sciences, 350 Shushanghu Road, Hefei, Anhui 230031, China

^f University of Science and Technology of China, Hefei 230026, China

ARTICLE INFO

Article history:

Received 25 August 2014

Received in revised form 22 May 2015

Accepted 2 June 2015

Available online 9 June 2015

Keywords:

Platinum
Iron
Conductivity
Resistance
Resistivity
Thermal
Electrical
Pressure
Temperature
High

ABSTRACT

The transport properties of matter at high pressure and temperature are critical components in planetary interior models, yet are challenging to measure or predict at relevant conditions. Using a novel flash-heating method for in-situ high-temperature and high-pressure thermal conductivity measurement, we study the transport properties of platinum to 55 GPa and 2300 K. Experimental data reveal a simple high-pressure and high-temperature behavior of the thermal conductivity that is linearly dependent on both pressure and temperature. The corresponding electrical resistivity evaluated through the Wiedemann–Franz–Lorenz law is nearly constant along the melting curve, experimentally confirming the prediction of Stacey for an ideal metal. This study together with prior first-principles predictions of transport properties in Al and Fe at extreme conditions suggests a broad applicability of Stacey's law to diverse metals, supporting a limit on the thermal conductivity of iron at the conditions of Earth's outer core of 90 W/mK or less.

© 2015 Elsevier B.V. All rights reserved.

1. Introduction

Knowledge of transport properties of planetary materials at relevant conditions of high pressure and temperature is vital for understanding planetary thermal histories and planetary properties such as magnetic fields (Goncharov et al., 2009a, 2015, 2010; Olson, 2013; Pozzo et al., 2012; Zhang et al., 2015). Efforts to constrain the transport properties of materials under extreme conditions require an understanding of the physical processes involved, which has been particularly elusive in the case of metals such as iron (de Koker et al., 2012; Pozzo et al., 2012; Stacey and Anderson, 2001; Stacey and Loper, 2007; Zhang et al., 2015). Many theories have been proposed to predict the transport properties of iron and its alloys at the conditions of planetary cores and to extrapolate from measurements at low pressure and temperature to core conditions (de Koker et al., 2012; Gomi et al., 2013; Pozzo et al., 2012; Seagle et al., 2013; Stacey and Anderson, 2001;

Stacey and Loper, 2007; Zhang et al., 2015). Among the theories used to predict transport properties in Earth's core, one is particularly notable in its simplicity and potential power. Due to Stacey (Stacey, 1992; Stacey and Anderson, 2001), it predicts that for pure ideal metals, electrical resistivity is constant along the melting curve at high pressure. Such a law would be a powerful tool in assessing planetary core transport properties, since measurements at low pressure melting points could be readily applied as constraints at the extreme pressure and temperature conditions of planetary cores (Stacey, 1992; Stacey and Anderson, 2001; Stacey and Loper, 2007).

Experimental validation of these models at high pressures and high temperatures is critically required but limited at present. The direct measurement of transport properties such as thermal and electrical conductivity at relevant conditions presents several difficulties. One major challenge is the creation of sufficient pressures and temperatures in the laboratory. Another is the application of techniques sensitive to transport properties at these conditions, such as electrical resistivity or thermal conductivity. In metals, thermal and electrical transport properties are closely connected through the Wiedemann–Franz–Lorenz law:

* Corresponding author at: Geophysical Laboratory, Carnegie Institution of Washington, 5251 Broad Branch Road NW, Washington, DC 20015, USA.

E-mail address: agoncharov@carnegiescience.edu (A.F. Goncharov).

$$k = L\sigma T \quad (1)$$

where k is the thermal conductivity, σ the electrical conductivity, T the temperature, and L a nominal constant of proportionality, the Lorenz number. Thus measurements of either thermal or electrical conductivity can determine both properties as long as L , and its variance with temperature and pressure (de Koker et al., 2012; French and Mattsson, 2014; Slack, 1964) is known. This study focuses on measurements of thermal transport.

Thermal transport properties can be established by measuring static temperature distributions or transient thermal responses of samples, either with direct measurements of temperature (e.g. using thermocouples or radiometry) or indirect measurements (e.g. of metal surface reflectivity). There have been numerous improvements in measuring thermal transport at high pressure and temperature using a laser-heated diamond-anvil cell and static temperature gradients (Konopkova et al., 2011; Manga and Jeanloz, 1997) or dynamic gradients established using pulsed (i.e. flash) laser heating (Beck et al., 2007; Goncharov et al., 2009a, 2010, 2012b). While flash heating is a traditional and sensitive approach for determining thermal transport properties of materials (Cape and Lehman, 1963; Hofmeister, 2006; Parker et al., 1961), measurements in the diamond anvil cell have only recently begun using a traditional approach of studying dynamic heat propagation across samples (Dalton et al., 2013; Hsieh et al., 2009; Ohta et al., 2012; Yagi et al., 2011). As these studies are currently limited to low temperature and have determined temperature perturbations indirectly, there is a need to develop methods that combine the approaches discussed above at combined high pressure and high temperature conditions and with direct temperature measurement.

Here we describe a new technique for measuring the propagation behavior of small heat disturbances across thin samples placed in the cavity of the diamond cell at high initial temperatures. Samples are preheated with continuous lasers to a desired temperature and then heated with a pulsed laser to generate a thermal perturbation. The experimental design reflects the configuration of traditional flash-heating thermal conductivity measurements, in which a suspended sample is pulse heated on one side, while the pulse arrival is measured on the opposite side. While this propagation can have a simple analytical solution (Cape and Lehman, 1963), in practice heat losses from the sample (traditionally in the form of thermal radiation) and other non-ideal features such as finite pulse duration, sample size, and laser spot size can complicate interpretation of data (Cape and Lehman, 1963; Hofmeister, 2006; Parker et al., 1961). Accurate thermal transport measurements can be made even with such practical concerns. In our case, we develop detailed finite element models of our experiments to interpret the data while including and evaluating non-ideal effects.

Initial experiments using our technique have been performed on platinum, a simple metal with a high-pressure phase diagram consisting of only the fcc-solid and liquid phases (Errandonea, 2013; Holmes et al., 1989; Kavner and Jeanloz, 1998). Iron, while having similar electrical conductivity to platinum (Slack, 1964), exhibits significantly more complex behavior at extreme conditions, including a variety of phase transitions and ferromagnetism. The physical properties of platinum and other simple metals at extreme pressure can be used as benchmarks in understanding multi-phase and electronically-complex metals such as Fe. Better systematic understanding of high-pressure and high-temperature transport behavior in metals can also improve assessments of transport in the complex alloys that comprise planetary cores. Pt is selected also for its low reactivity and incompatibility with impurities, which can promote regularity across different experiments (Slack, 1964).

2. Experimental method

We placed a thin foil of Pt in a transparent insulating medium of NaCl or KCl in the cavity of the diamond cell (Fig. 1a). Foils were 99.95% platinum with an initial thickness of 4 μm , purchased from the GoodFellow Corporation. Foil thickness was verified by positioning it between diamond anvils at ambient conditions and measuring the anvil-to-anvil distance with white light interferometry (see below). NaCl and KCl were loaded as dry powder compressed into thin plates, which were placed on either side of the foil during loading. Pressure was measured by ruby fluorescence (Mao et al., 1986).

The foil is heated from both sides by a continuous infrared laser to a desired temperature prior to pulsed laser heating. Laser heating spot size was controlled with a series of lenses (Fig. 2) including a beam shaper to flatten the intensity distribution of the spot (Goncharov et al., 2009b). Due to the diameter of laser heating spots ($\sim 10 \mu\text{m}$ diameter) and the thickness of our sample foils ($\sim 4 \mu\text{m}$), conduction in the heated portion of the foil is nearly in one dimension. Temperature in this region is nearly homogeneous (Fig. 1b). The hottest region of the foil surface dominates emission, and so measured temperature histories are localized to the region of highest temperature. Also, foil thermal conductivity increases with temperature (Slack, 1964) so that the initial arrival of heat perturbations (to which our conductivity measurements are most sensitive) occurs in the region of highest temperature. These features ensure a self-consistent measurement of thermal conductivity and its associated temperature.

Both sides of the sample are imaged to a spectrometer (Princeton Instruments f/4 using a 150 grooves/mm grating) coupled to a streak camera (Sydor ROSS 1000), which is used to record emission spectra from the sample in a time-resolved fashion (Figs. 2 and 3). Every 1 ms (at a rate of 1 kHz), the streak spectrometer collected emission during a time window of 3–10 μs , during which the emission spectrum from the sample was swept across the CCD-based detector to produce a spectrogram of emission versus time 3–10 μs long. Following a single sweep, little to no emission could be discerned in the CCD. Following many stacked sweeps, emission accumulated on the CCD to a sufficient degree that temperature could be determined at each time in the image by fitting the local emission spectrum to a Planck function.

In a given spectrogram, emission was measured from either side of the foil or from both sides simultaneously using color filtering to split the spectral window (165 nm range) to include emission from both sides. Data character was highly reproducible in repeated measurements. In view of this, the best temperature precision was obtained by using the full spectral window to record emission from a given side of the sample and collecting two spectrograms in sequence with identical heating, each observing a different side of the sample.

Continuous laser power was raised until an emission signal was detected (typically possible for $T > 1600 \text{ K}$) and then adjusted to reach a desired temperature. The total CW heating time ranged from up to 10 s at low temperatures to less than 1 s at high temperatures (Fig. 3a). Initially, emission and temperature were constant in time in the spectrograms. CW laser power at each side of the sample was independently adjusted until the temperatures determined on each side were similar to within $\sim 100 \text{ K}$. Then, a second laser firing short pulses (several μs duration) at 1 kHz and synchronized with streak image collection was delivered to one side of the sample. This produced a time-dependent perturbation in the thermal emission intensity and fitted temperature on both sides of the sample. We utilize the minimum pulse amplitudes sufficient to accurately detect the temperature perturbations, which are usually less than 200 K. The timing of data

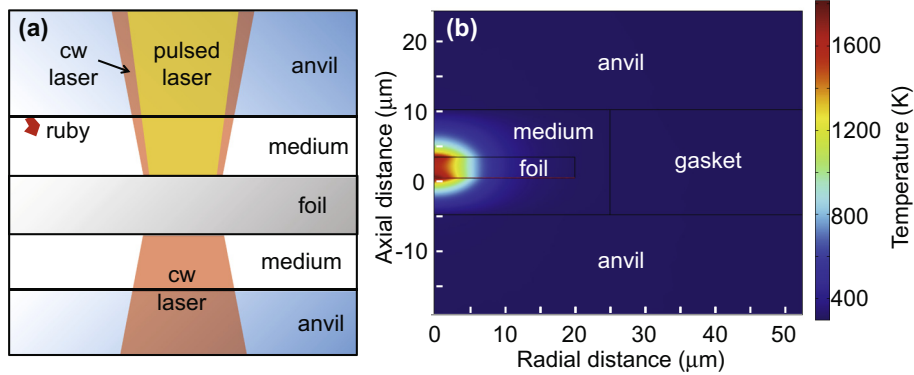


Fig. 1. Configuration of the laser-heated diamond anvil cell experiment. A schematic of the sample and laser illumination is shown in (a) while an instantaneous snapshot from an axially-symmetric finite-element model of a transiently-heated sample is shown in (b). Laser heating energy was delivered to one or both sides of a metal foil suspended in the diamond cell cavity, which was surrounded by a transparent medium and contained between the anvils and a metallic gasket (Re). Alignment of the three laser spots was done at transparent areas of the sample (e.g. radial distance of 20–25 μm in b).

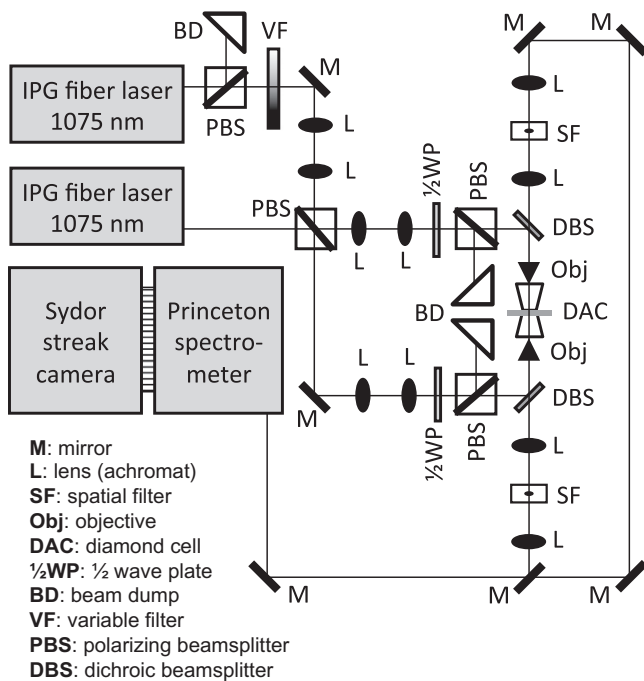


Fig. 2. Apparatus for thermal conductivity measurements. Samples were confocally imaged to a spectrometer (Goncharov et al., 2009b). The lower fiber laser continuously heats the sample foil from both sides to raise its initial temperature, while the upper fiber laser operates in pulsed mode to deliver a heat pulse on one side of the sample. Continuous heating power is balanced to produce equal temperature on both sides of the foil using polarization techniques, prior to initiation of pulsing. The pulsed heating laser is polarized to strike only one side of the sample, while power was controlled through various filters. Time resolved spectroscopy of emission was made using a streak camera (Sydor Ross 1000) coupled to a spectrometer (Goncharov et al., 2012a). Both sides of the foil could be viewed in the detection system simultaneously.

recorded from either side of the sample differed due to a combination of optical delay and spatial separation of images on the streak camera photocathode, and was measured using a short-pulse (150 ps) broadband light source (Goncharov et al., 2012a; McWilliams et al., 2015) focused at the sample plane.

Emission data was corrected for camera sensitivity variations in time and wavelength, as well as for the transmission function of the optical system, and was referenced to a tungsten-filament NIST-traceable calibration lamp with a known spectrum. Other

distortions in the streak image such as non-orthogonality and non-linearity of time and wavelength axes were completely corrected for in the data.

Emission was fitted assuming wavelength-independent emissivity, as plausible emissivity variations with wavelength (Haynes, 2011) did not have a significant effect on the results. In a first round of fitting, temperature and emissivity were free parameters. Since temperature perturbations were small, it was reasonable to consider the emissivity constant during the experiment. An average value of emissivity was determined, and emission was re-fit assuming constant emissivity. This approach ensured accurate determination of the absolute temperature, while eliminating random noise in the temperature time histories to produce precise data on the relative temperature change with time. With this approach, the timing and form of small temperature disturbances could be reliably measured.

Sample dimensions were characterized in-situ for accurate finite element modeling. Radial dimensions (of foil and gasket hole) were determined by optical microscopy. The *in-situ* foil thickness was determined using the platinum equation of state (Dorogokupets and Dewaele, 2007; Jin et al., 2011). Pressure medium thicknesses were determined using white light interference microscopy and the index of refraction under pressure (Johannsen et al., 1997), which also provided a second test of the *in-situ* foil thickness. This value was found to be consistent with that determined from the equation of state and initial thickness. Foil expansion upon heating is small (<2%) compared to the thickness uncertainty (5–10%, Table 1) in part due to sample confinement which limits free expansion and instead produces thermal pressure (Dewaele et al., 1998; Goncharov et al., 2007).

Samples were visually inspected for damage during experiments to ensure sample metrology was not affected by heating. If damage occurred, data were discarded and pristine regions of the foil were studied. Lateral dimensions of foils are much greater than their thickness and also much greater than the size of the laser heated area so that a move to an undamaged region preserves the local sample's ideal geometry. Upon increasing laser power (both in CW and pulse modes), samples often exhibited a sudden increase in emission amplitude and temperature. Temperature typically jumped from near 2000 K to over 3000 K and exceeded the melting points of the foil and medium (Boehler et al., 1996, 1997; Errandonea, 2013; Kavner and Jeanloz, 1998; McWilliams et al., 2015). We attribute this to laser absorption in the pressure medium upon melting (Boehler et al., 1996, 1997). Since laser energy is not deposited wholly at the foil surface in this

interpretation and since samples were usually damaged, experiments having this character were not used.

3. Finite-element modeling

Heat transfer within the DAC was simulated numerically by solving for the transient heat equation with appropriate boundary conditions using a finite element method (Beck et al., 2007; Goncharov et al., 2009a, 2010, 2012b; Konopkova et al., 2011;

Montoya and Goncharov, 2012). The transient heat conduction equation reads:

$$\rho C_p \frac{\partial T}{\partial t} + \nabla \cdot (-k \nabla T) = Q, \quad (2)$$

where ρ is the density, C_p the heat capacity at constant pressure, k the thermal conductivity, and Q any volumetric heat source. Because the laser energy is absorbed at the surface of the foil, heat input is modeled as a heat flux boundary condition rather than as a volumetric source, and hence $Q=0$. The boundary conditions express continuity of heat flux at the interface of two adjacent sample domains. The laser heat source f is expressed at the boundaries between the foil and medium as:

$$-\vec{n}_{sam} \cdot (-k_{sam} \nabla T_{sam}) - \vec{n}_{med} \cdot (-k_{med} \nabla T_{med}) = f \quad (3)$$

where \vec{n} is the surface normal unit vector and subscripts *sam* and *med* indicate the side of the boundary corresponding to the metal sample and pressure medium, respectively. Eq. (2) is solved in each subdomain (sample, medium, gasket, diamond) with appropriate values of ρ , C_p and k for each material (Table 1). Model geometry has been simplified to a 2D problem with axial symmetry (coordinates r, z), with the axis coinciding with the center of the laser foci, sample foil, and DAC cavity.

Simulation of the temperature distribution is performed in two steps. First, the continuous heating is modeled by solving the steady-state heat equation:

$$\nabla \cdot (-k \nabla T) = 0 \quad (4)$$

with the boundary condition at the laser absorbing interfaces given as:

$$f = \frac{p}{\pi R^2} e^{-(1/2)(r^2/R^2)} \quad (5)$$

where p is the absorbed laser power and R is the radius of the laser focus (μm), which has a Gaussian intensity distribution. Initially:

$$p = p_{CW} \quad (6)$$

where p_{CW} is the continuous laser power, a constant that was different on each side of the sample and was adjusted until the foil surface achieved a peak temperature equivalent to the observed temperature prior to pulse arrival. The steady-state solution thus obtained was stored and used as a starting point for the solution employing the transient heat equation (Eq. (2)) and pulsed heating with laser power given by:

$$p = p_{CW} + p_{PS} \quad (7)$$

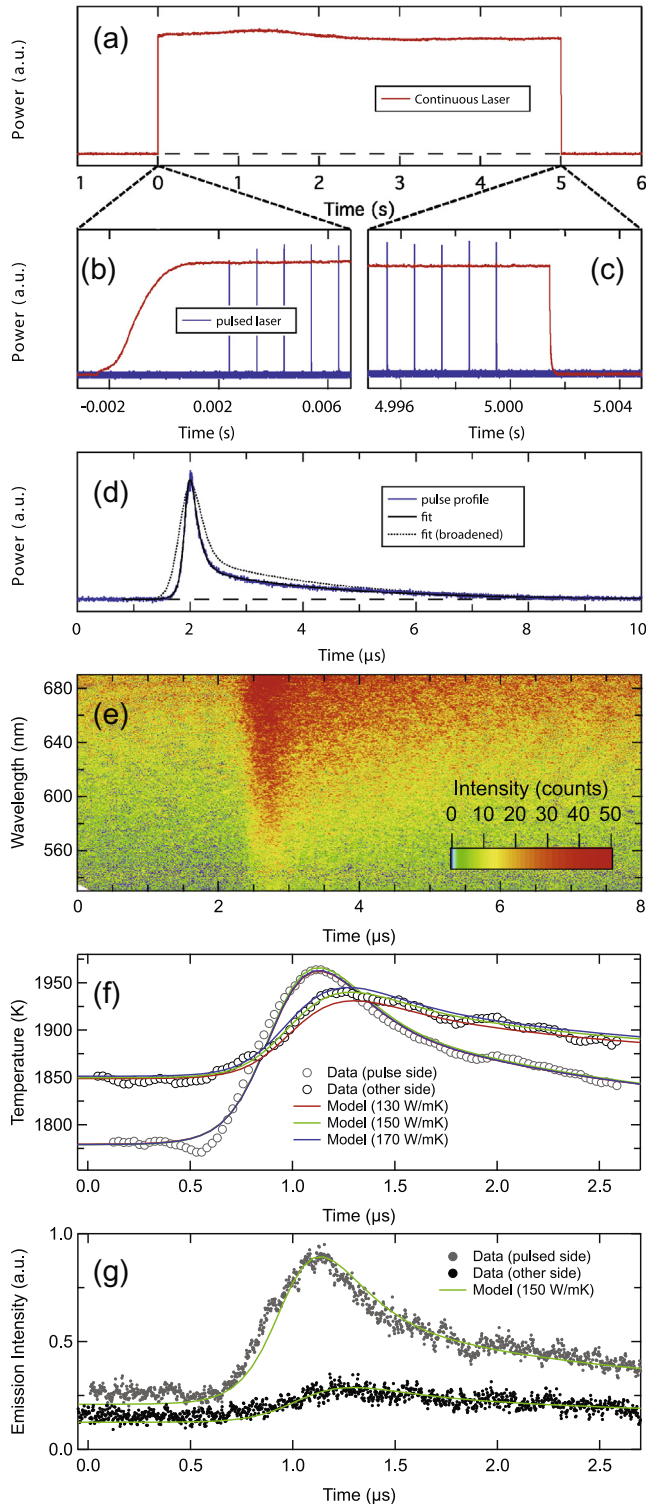


Fig. 3. Design of flash heating thermal conductivity measurements. Data in (a–d) were collected with a photodiode and oscilloscope, and in (e–g) with a streaked spectrometer. In this representative experiment on Pt at 48 GPa (Table 1), a CW laser heats both sides of the foil sample for 5 s (a) while a pulsed laser operating at 1 kHz heats one side. CW and pulsed laser shut on and off (b–c) is controlled by electronic modulation and fast shuttering. Individual laser pulses have a profile shown in (d), which has a sharp rise to a peak followed by exponential decay; for finite element modeling this was fit by an analytical function, which was sometimes broadened to account for instrumental timing jitter during data acquisition. Synchronized with the laser pulses, a streak camera records thermal emission spectrograms from the sample (e); here the record is taken from a single side of the foil and based on accumulation from ~ 5000 stacked spectrograms. The time-resolved temperature (f) and band-averaged (550–692 nm) emission intensity (g) are fit using finite element models (solid curves). In (f) random errors are smaller than the symbols while systematic errors are ~ 50 K; in (g) point scatter represents random error. Here initial temperatures on either side of the foil differ by ~ 75 K and the range of temperatures during the experiment is ~ 175 K; an average temperature is reported for each experiment (Figs. 5 and 6).

Table 1

Properties of samples used in finite element modeling. Foil thicknesses were known to 5–10% precision. The equations of state for Pt, NaCl, and KCl were used (Dewaele et al., 2012; Dorogokupets and Dewaele, 2007; Jin et al., 2011). Input parameters that do not vary with pressure are as follows: thermal conductivity k of diamond (1000 W/mK) and Re (48 W/mK); density ρ of diamond (3500 kg/m³) and Re (21,020 kg/m³); and the specific heat at constant pressure C_p of diamond (630 J/kg K), Re (140 J/kg K), NaCl (864 J/(kg K), KCl (690 J/kg K), and Pt (135 J/kg K).

P (GPa)	Medium	Sample thickness (μm)	Chamber thickness (μm)	Pulseside thickness (μm)	Opposite thickness (μm)	Medium density (kg/m ³)	Pt density (kg/m ³)
35	NaCl	3.25	18.5	8.3	7.0	3633	23,670
48	NaCl	3.00	16.4	7.4	6.0	3929	24,340
50	KCl	3.00	16.4	7.4	6.0	4082	24,440
55	NaCl	2.90	15.4	7.0	5.5	4038	24,670

where p_{ps} is a time dependent function determined by fitting the power profile of the laser pulse to a suitable analytical function (Fig. 3d).

Modeling yielded temperature distributions in space and time for the sample, medium, and nearby regions of the gasket and anvils (Fig. 1b). In addition to reading sample temperatures from the simulations directly, the corresponding emission was predicted. Temperature profiles within a given radius around the laser heated spot were used to calculate total emission based on integration of Planck's function over 550–692 nm (the spectral range used to measure emission intensity) and over the heated spot. The radius of integration was controlled by our spatial filtering system (Fig. 2) and was typically ~ 10 microns, such that most emission signal from the heated sample area entered our detection system. We compare observed temperature and emission with simulated values during refinement of our simulations (Fig. 3).

The geometry of the model and input constants at all pressures are listed in Table 1. For the diamond anvils and gasket (Re), ambient values of ρ , C_p and k are used. The high-pressure densities of Pt and the pressure medium are taken from their equations-of-state (Dewaele et al., 2012; Dorogokupets and Dewaele, 2007; Jin et al., 2011). The value of C_p used for Pt was determined at the conditions of the experiments from the equations of state (Dorogokupets and Dewaele, 2007; Jin et al., 2011) and was found to be nearly the ambient value; C_p for the pressure medium is taken as the ambient value and results were not found to be sensitive to this choice. The most important parameters affecting the resulting values of thermal conductivity are the thickness of the sample and the relative timing of temperature histories. The above parameters were generally treated as constants during modeling, but were also varied in some cases to test model sensitivity to the different parameters and to evaluate associated uncertainties.

Several parameters were treated as variables during the modeling in order to reproduce the observed temperature histories: p of the laser for both sides of the foil, R of the laser focal spots, k of the pressure medium, and k of the sample. Values of p and R were estimated from values observed in experiments and were fine-tuned to best match the simulation to the data. The k values were usually treated as invariant with temperature; introducing temperature dependences did not significantly affect the results. For example, we tested a temperature variation in k for Pt similar to that seen at ambient pressure (Slack, 1964) but scaled by a constant multiple chosen to best match the high-pressure data, and found that the difference in measured k was less than 6% compared to that obtained assuming a constant value. This difference is negligible given our overall uncertainty in k ($\sim 20\%$).

In our modeling, it is observed that k of the pressure medium primarily affects the rate of temperature decay after extinction of the laser pulse, whereas k of the foil and R have a mutual influence on the rise of the thermal pulse on the opposite side of the foil. Therefore, the simulations were performed in several iterative steps in search of a best value for k of Pt. First, a k of the pressure medium was found that reproduced approximately the temperature decay following the perturbation. Then, for a given R , k of

the sample was adjusted until the rise of the thermal pulse on the opposite side of the sample and the temperature difference across the sample were matched. Small iterative adjustments of the variables were then performed to achieve the best fit to the experimental data (Fig. 3). To test the sensitivity of the models the computation was repeated for several values of the laser spot size and for systematic variations in other parameters. Best values and uncertainty were assessed from the compilation of models thus produced.

Radiative heat losses from the sample, an important feature of traditional flash-heating measurements (Cape and Lehman, 1963; Hofmeister, 2006), are insignificant in the present case. Heat losses by radiative transfer can be included as a boundary condition in Eq. (5) as:

$$f = \frac{p}{\pi R^2} e^{-(1/2)(r^2/R^2)} + \varepsilon \sigma_B (T_{amb}^4 - T^4) \quad (8)$$

where ε is the surface emissivity, σ_B the Stefan–Boltzmann constant and $T_{amb} = 300$ K. We find that radiative heat losses are negligible compared to losses by conductive heat transfer, so conduction alone sufficiently describes the thermal behavior of samples as previously observed (Dewaele et al., 1998; Manga and Jeanloz, 1997; Montoya and Goncharov, 2012).

Because of instrumental jitter in the timing of the spectrogram relative to the laser pulse from sweep to sweep, thermal perturbation time histories in stacked spectrograms are broadened in our data, compared to those predicted assuming a pulse at constant timing. Assuming the distribution of timings is Gaussian, we account for this effect by a convolving the single-pulse intensity curve with a Gaussian broadening function prior to modeling (Fig. 3d). While improving model agreement with our data, inclusion of instrumental broadening effects had a minor effect on the results.

4. Reference model: ideal flash heating

Finite-element analysis of flash heating was tested by simulating an ideal flash heating experiment for which there is an analytical solution, that is, one with no heat loss from the sample, one-dimensional heat propagation, and an instantaneous impulse (Fig. 4). This artificial case was modeled for a Pt foil similar to that used here, with heat loss prevented, the diameter of the laser spot increased to twice the plate diameter, and the duration of the input pulse was reduced to a few nanoseconds so that it was nearly instantaneous on the experimental timescale. In this ideal configuration, heat wave arrival at the opposite surface from pulsed heating is related to the thermal diffusivity κ as (Cape and Lehman, 1963; Parker et al., 1961):

$$\kappa = 1.37 \frac{d^2}{\pi^2 \tau_{1/2}} \quad (9)$$

where d is the sample thickness, $\tau_{1/2}$ is the time difference between the pulse and the halfway rise time of temperature on the opposite side, and:

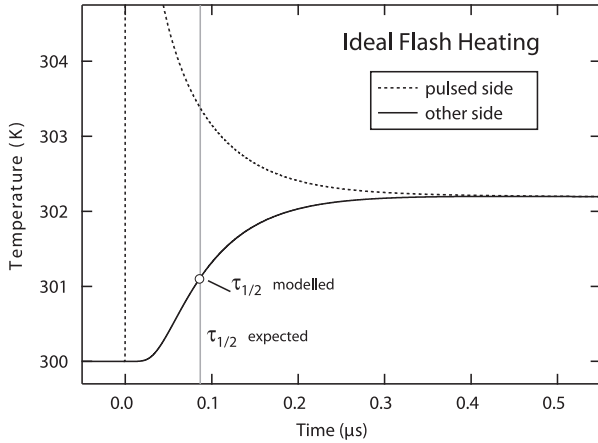


Fig. 4. Finite element simulation of a hypothetical ideal flash heating experiment in the diamond cell. Similar to our actual experiment (Fig. 1), a Pt sample of 4 μm thickness and 40 microns diameter is used, which is initially at room temperature with $\kappa = 2.57 \times 10^{-5} \text{ m}^2/\text{s}$. Foil heat losses are eliminated. The foil is struck on one face at time zero with a short pulse a few nanoseconds in duration and providing nearly constant intensity over the foil surface ($R = 80 \text{ μm}$, Eq. (5)). The opposing-face temperature rises halfway to its maximum value $\sim 85 \text{ ns}$ later yielding $\kappa = 2.59 \times 10^{-5} \text{ m}^2/\text{s}$ through Eq. (9), closely reproducing the input value.

$$\kappa = \frac{k}{\rho C_P} \quad (10)$$

Determining κ from the simulated temperature history with Eq. (9) yields a value within 1% of the input value, affirming the accuracy of at least a simplified version of our finite-element analysis. The delay between the laser pulse and the temperature rise on the opposite side of the sample ($\sim 100 \text{ ns}$) is comparable to that observed in real experiments (Fig. 3). However, in real experiments, heat losses from samples lead to temperatures that decrease in time rather than approach an asymptotic value (Cape and Lehman, 1963) (e.g. Fig. 3g).

5. Experimental results

The data on Pt show a general trend of increasing k with pressure and temperature. The values show a clear enhancement in k over ambient pressure and temperature data, and are the highest yet measured in Pt, resolved at 2.1 sigma.

To analyze our results and transform between thermal and electrical conductivity, we developed a simple model to fit the available data. In our analysis, we use the Wiedemann–Franz–Lorenz relation (Eq. (1)) to convert between thermal and electrical conductivity. Lattice contributions to thermal conduction are not included in Eq. (1) and are substantially less than electronic contributions in metals (de Koker et al., 2012; Stacey and Anderson, 2001) so are ignored in the present analysis. In the case of Pt, L depends on temperature (Slack, 1964) in a manner that can be represented as a double-exponential function (Fig. 6g)

$$L_{\text{Pt}} = \beta - \alpha_1 \exp(-\tau_1 T) - \alpha_2 \exp(-\tau_2 T) \quad (11)$$

where $\beta = 3.18$, $\alpha_1 = 0.839$, $\alpha_2 = 1.29$, $\tau_1 = 1.23 \times 10^{-3}$, $\tau_2 = 1.07 \times 10^{-2}$, and L is in $10^{-8} \text{ V}^2/\text{K}^2$ and T in K. We find good model fits in the present case are obtained by assuming L is independent of pressure; measurement of L under pressure is needed to assess any systematic errors due to this assumption. Values of L for Pt are similar to the theoretical value of $2.44 \times 10^{-8} \text{ V}^2/\text{K}^2$ for a metal following a free-electron model (Fig. 3g) but are greater at relevant temperatures by $\sim 30\%$.

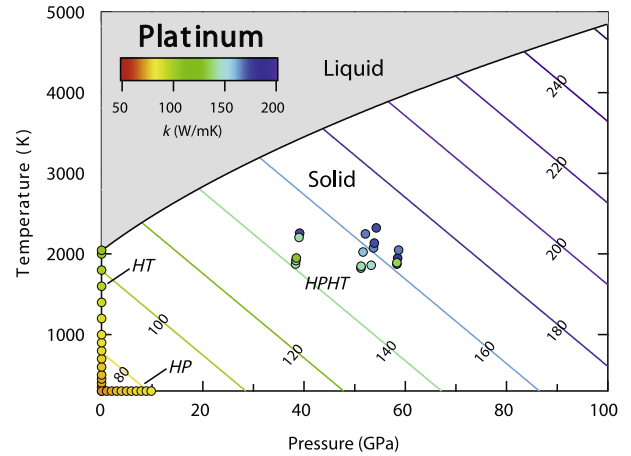


Fig. 5. Thermal conductivity map for solid platinum. Data (colored circles) are from this study (HPHT, plot center), high temperature (HT, left axis) (Slack, 1964), and high pressure (HP, bottom axis) (Bridgman, 1952). Contours, based on a global fit to the data (Eq. (15)), are labeled with corresponding k values. The melting curve is the solid black line based on extrapolation of recent melting measurements to 28 GPa (Errandonea, 2013). For the present study, uncertainties in individual measurements of k are 20 W/mK; pressure uncertainty is $\sim 1 \text{ GPa}$; random temperature uncertainties are 50 K; possible systematic temperature errors due to Pt emissivity variation with wavelength (Haynes, 2011) are $\sim 125 \text{ K}$ and, if included in our analysis, do not have a significant affect on the results. (For interpretation of the references to color in this figure legend, the reader is referred to the web version of this article.)

We fit our present measurements of thermal conductivity (k) in Pt with a simple planar fit in pressure (P) – temperature (T) space:

$$k = aP + bT + c \quad (12)$$

where a , b , and c are constants. This form is selected considering that k increases nearly linearly with T at constant P (Slack, 1964) (Fig. 6b), and nearly linearly with P at constant T (Bridgman, 1952) (Fig. 6d). In this model resistivity ($1/\sigma$) varies inversely with pressure at constant temperature as:

$$1/\sigma \sim 1/P \quad (13)$$

This form reproduces the behavior of resistivity in many metals under pressure, including Pt (Bridgman, 1952) (Fig. 6c) and ϵ -Fe (Gomi et al., 2013; Seagle et al., 2013). At constant pressure, resistivity varies with temperature as:

$$1/\sigma \sim \exp(T) \quad (14)$$

This form ideally describes the data for platinum (Slack, 1964), and is not in practice significantly different from the often-used relationship for metals $1/\sigma \propto T$ (de Koker et al., 2012; Seagle et al., 2013; Stacey and Anderson, 2001). Thus, this simple model for the thermal and electrical conductivity is empirically justified.

A small thermal pressure is included in the present measurements prior to fitting. This is assumed to be 30% of the isochoric thermal pressure (Dewaele et al., 1998; Goncharov et al., 2007) taken from equation-of-state data on Pt (Dorogokupets and Dewaele, 2007; Jin et al., 2011), and equals $\sim 2 \text{ GPa}/1000 \text{ K}$.

The above model is least-squares fitted to the available data for platinum (Figs 5 and 6). In addition to data from this study at combined high-temperature and high-pressure, we include an ambient-pressure survey of thermal conductivity at high temperature (up to 2047 K) (Slack, 1964) as well as resistivity data at ambient temperature and high pressure (up to 10 GPa) (Bridgman, 1952). When all three datasets are included in our fit, we refer to the result as the ‘global fit’.

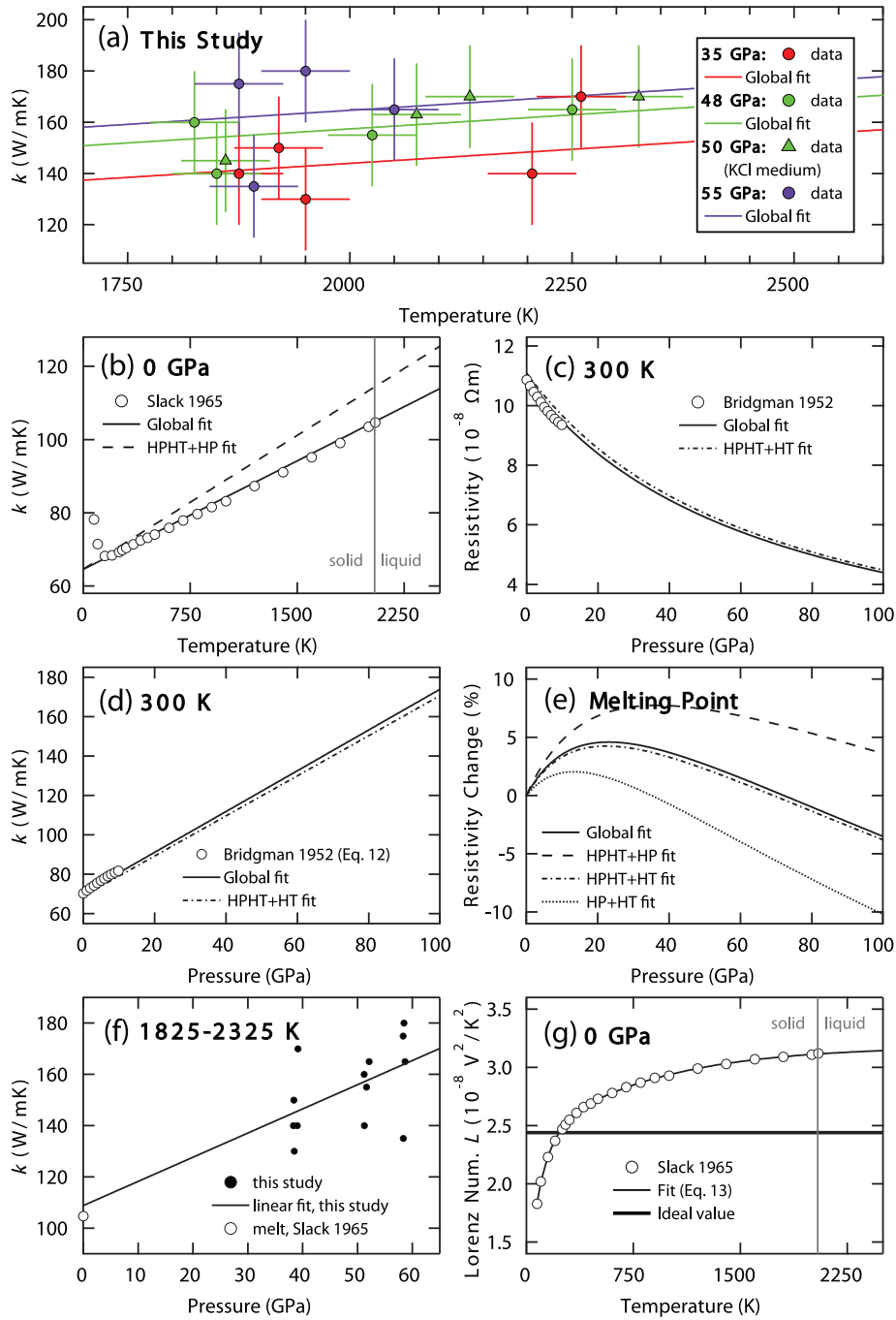


Fig. 6. Summary of results for platinum. (a) Present results at high pressure and temperature (HPHT) are compared to results of global fit to HPHT, HT (Slack, 1964), and HP (Bridgman, 1952) data. The pressure medium was NaCl unless otherwise indicated. Both data and model curves account for thermal pressure (room-temperature values are listed). (b) k vs. T at ambient pressure from HT data, global fitting, and fitting that excluded HT data. (c and d) Resistivity ($1/\sigma$) and k vs. P at ambient temperature from HP data, global fitting, and fitting that excluded HP data. (e) Percent change in resistivity along the melting curve with increasing pressure in four types of fit (global fit and three fits excluding one dataset each). (f) k vs. P at $T \sim 2000$ K, showing HPHT measurements fit to a linear function that extrapolates to the value of k at melting at ambient pressure (Slack, 1964) (g) L vs. T (Slack, 1964) with double-exponential fit (Eq. (11)) and the theoretical value (de Koker et al., 2012; Stacey and Anderson, 2001).

In addition to least-squares fitting to all three datasets described above, individual measurements or sets of measurements were included and excluded during fitting to test fit stability and sensitivity to certain datasets or data points. Of the three sets of data used in the fit, any two datasets were sufficient to define the fit. That is, exclusion of any one dataset had a minor effect on fit results. Notably, the unfit dataset was well predicted by a fit of the other two (Fig. 6b–c). Our high-pressure measurements

are thus consistent with data at low pressure (Bridgman, 1952; Slack, 1964). This can be further seen in Fig. 6f, where our high temperature data are found to compare well with those at similar temperature and low pressure (Slack, 1964).

When the present results are fit alone, the trend of increasing k with pressure and temperature (Fig. 5) is qualitatively reproduced, but the fit does not predict the previous ambient P and ambient T measurements with good accuracy. A notable exception is that a fit

to the present data alone accurately predicts the thermal and electrical conductivity at melting at ambient pressure. This is because the pressure variation of transport properties is well resolved in our data at temperatures similar to the ambient melting point (Fig. 6f).

Our data and model thus permit a self-consistent and simple description of transport in platinum at extreme conditions. Thermal and electrical conductivities in solid platinum based on our global fit can be represented as:

$$k_{\text{Pt}} = 1.03P + 0.0198T + 64.5 \quad (15)$$

and

$$\sigma_{\text{Pt}} = \frac{k_{\text{Pt}}}{TL_{\text{Pt}}} \quad (16)$$

where k is in W/mK, σ is in S/m, P is in GPa, T is in K, and L (Eq. (11)) is in V^2/K^2 . This fit is not valid below 150 K, where a sharp change in the behavior of the transport properties occurs (Slack, 1964) (Fig. 6b). Eqs. (15) and (16) may be used to estimate properties of the liquid beyond the melting curve (Fig. 5), though a decrease in k and σ on melting (Wilthan et al., 2004) may need to be considered.

6. Discussion

The consistency between available transport measurements in Pt at high pressure and temperature and the successful global description of these data with a simple model suggest that platinum is an ideal system in which to test theories of transport in metals at extreme conditions (de Koker et al., 2012; Gomi et al., 2013; Pozzo et al., 2012; Seagle et al., 2013; Stacey and Anderson, 2001; Stacey and Loper, 2007; Zhang et al., 2015).

The global fit to the transport data on Pt as well as three partial fits predict nearly-constant resistivity along platinum's melting curve (Fig. 6e). From the global fit, resistivity at melting is $61.6 \pm 1.5 \times 10^{-8} \Omega\text{m}$ and deviates by no more than 4.5% from a constant value from zero to 100 GPa (Fig. 6e) and from 2000 to 5000 K (Fig. 5). This contrasts with a change in resistivity of nearly an order of magnitude over the same pressure range at constant temperature (Fig. 6c) or the same temperature range at constant pressure (Slack, 1964). Also along the melting curve the Lorenz number is constant to within 1% at $3.17 \times 10^{-8} \text{V}^2/\text{K}^2$. The combined effects of increasing pressure and temperature along the melt curve, which have opposing effects on resistivity (to decrease and increase resistivity, respectively), combine to maintain the resistivity at a constant value at melting.

The arguments of Stacey (Stacey, 1992; Stacey and Anderson, 2001; Stacey and Loper, 2007) put this effect on a firm physical foundation. Stacey noted that the derivative of electrical resistivity with pressure could have the same form as Lindemann's law for the derivative of melting temperature with pressure, leading to the conclusion that resistivity is invariant along melting curves for simple metals. Thus Stacey's theory can be thought of as an extension of Lindemann's law and is here referred to as Stacey's law.

There are reasons to expect that Stacey's law is accurate for a number of transition metals. In addition to our results on Pt, this law also appears to be followed in theoretical predictions for Al (Vlček et al., 2012) and Fe (de Koker et al., 2012; Zhang et al., 2015) (Fig. 7). Together, these results demonstrate the reasonable accuracy of this model for predicting thermal and electrical conductivity at the melting curve for ideal metals, and support proposed extensions of this law to impure and nonideal metals (Stacey and Anderson, 2001; Stacey and Loper, 2007). Verification of Stacey's Law for Fe remains to be investigated experimentally.

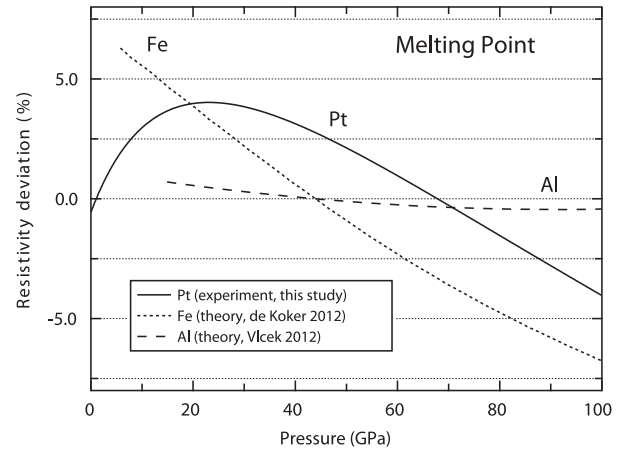


Fig. 7. Deviation from Stacey's law of constant resistivity at melting. Results for Pt (this study), Fe (Anzellini et al., 2013; de Koker et al., 2012) and Al (Vlček et al., 2012) are shown. Deviations are computed so the range is centered on zero.

7. Conclusions

Thermal conductivity of platinum has been determined at temperatures of 1800–2300 K and pressures up to 55 GPa using a pulsed laser heating technique in the diamond anvil cell combined with finite element modeling of heat transfer. The results confirm an increasing conductivity with pressure and temperature in Pt, previously seen in studies near ambient pressure and temperature. We find that electrical resistivity at melting, determined through the Wiedemann–Franz–Lorenz law, is largely invariant with pressure up to 100 GPa, as predicted by Stacey for a simple metal (Stacey, 1992; Stacey and Anderson, 2001).

Stacey's law of constant resistivity along the melting curve for metals can be used to predict transport properties of Fe at core conditions, by taking the measured value of resistivity at ambient-pressure melting ($1.35 \times 10^{-6} \Omega\text{m}$), and applying this to Earth's core, where temperatures are close to the melting point (3750–4970 K) (Stacey and Anderson, 2001). Assuming the ideal value of the Lorenz number for a free-electron metal, thermal conductivity is thus estimated to be 68–90 W/mK for Fe at core conditions. Adjustment for impurity content, temperature offset from the melting curve, and deviations from pure metal behavior due to the complex band structure of Fe act cumulatively to lower thermal conductivity and imply an upper bound on outer core thermal conductivity of ~ 63 W/mK (Stacey and Anderson, 2001; Stacey and Loper, 2007).

The present work confirms that Stacey's law can be accurate for simple metals and thus supports the primary foundation of the above constraints. Observed deviations from this law – less than 4.5% in Pt, with similar small deviations predicted for Al (Vlček et al., 2012) and Fe (de Koker et al., 2012; Zhang et al., 2015) – do not warrant a serious readjustment of this constraint. That evidence for this law appears in quite dissimilar transition metals suggests it may have widespread applicability, and it should be tested for in other metals.

While further investigations into the validity and physical origin of Stacey's law should be made in future studies, attention should be paid to the assumptions (Stacey and Anderson, 2001; Stacey and Loper, 2007) that permit its application to planetary cores. Of primary importance is the assumed value of conductivity at the ambient-pressure melting point, which can differ significantly between experimental and theoretical studies (de Koker et al., 2012; Stacey and Anderson, 2001). The Lorenz number L for Fe at high pressure and temperature also needs to be accurately

determined; use of the theoretical value for a free-electron metal (Stacey and Anderson, 2001; Stacey and Loper, 2007) is of questionable validity considering the wide range of values seen in transition metals (French and Mattsson, 2014; Slack, 1964) and the proposed significance of electron–electron scattering at high temperatures (Zhang et al., 2015). Measurements of Fe thermal conductivity at *in-situ* high-pressure and temperature as well as studies on other transition metals are needed to improve constraints on this important problem.

Our measurements finally have a practical implication for planetary materials' transport measurements. Platinum is a preferred electrode material in measurements of electrical conductivity at extreme conditions, for example in studies on water (Okada et al., 2014), iron (Seagle et al., 2013; Shimizu et al., 2001), silicate perovskite (Li and Jeanloz, 1990) and hydrogen (Eremets and Trojan, 2009). As electrode properties can bias such measurements (Huang et al., 2007) the results of this study permit evaluation and removal of electrode contributions to transport measurements, both at high pressure and high temperature.

8. Author contributions

All authors contributed to experimental design and execution, and to the writing this manuscript. Z.K. and A.F.G. loaded and characterized samples. R.S.M. reduced the raw data. Z.K. conducted finite element simulations.

Acknowledgements

We thank N. deKoker for providing us with numerical results and suggestions, N. Gomez-Perez and T. Komabayashi for helpful discussions, and George Helffrich and an anonymous reviewer for their comments on our manuscript. This work was supported by the NSF Major Research Instrumentation program, NSF EAR-1015239 and NSF EAR/IF-1128867, NSF EAR/IF, the Army Research Office (56122-CH-H), the Carnegie Institution of Washington, the University Of Edinburgh, and the British Council Researcher Links Programme.

References

- Anzellini, S., Dewaele, A., Mezouar, M., Loubeyre, P., Morard, G., 2013. Melting of iron at earth's inner core boundary based on fast X-ray diffraction. *Science* 340, 464–466.
- Beck, P., Goncharov, A.F., Struzhkin, V.V., Militzer, B., Mao, H.K., Hemley, R.J., 2007. Measurement of thermal diffusivity at high pressure using a transient heating technique. *Appl. Phys. Lett.* 91.
- Boehler, R., Ross, M., Boercker, D.B., 1996. High-pressure melting curves of alkali halides. *Phys. Rev. B* 53, 556–563.
- Boehler, R., Ross, M., Boercker, D.B., 1997. Melting of LiF and NaCl to 1 Mbar: systematics of ionic solids at extreme conditions. *Phys. Rev. Lett.* 78, 4589–4592.
- Bridgman, P.W., 1952. The resistance of 72 elements, alloys and compounds to 100,000 Kg/cm². *Proc. Am. Acad. Arts Sci.* 81, 165–251.
- Cape, J.A., Lehman, G.W., 1963. Temperature and finite pulse-time effects in flash method for measuring thermal diffusivity. *J. Appl. Phys.* 34, 1909.
- Dalton, D.A., Hsieh, W.-P., Hohensee, G.T., Cahill, D.G., Goncharov, A.F., 2013. Effect of mass disorder on the lattice thermal conductivity of MgO periclase under pressure. *Sci. Rep.* 3.
- de Koker, N., Steinle-Neumann, G., Vlček, V., 2012. Electrical resistivity and thermal conductivity of liquid Fe alloys at high P and T, and heat flux in Earth's core. *Proc. Natl. Acad. Sci. U.S.A.* 109, 4070–4073.
- Dewaele, A., Fiquet, G., Gillet, P., 1998. Temperature and pressure distribution in the laser-heated diamond-anvil cell. *Rev. Sci. Instrum.* 69, 2421–2426.
- Dewaele, A., Belonoshko, A.B., Garbarino, G., Occelli, F., Bouvier, P., Hanfland, M., Mezouar, M., 2012. High-pressure–high-temperature equation of state of KCl and KBr. *Phys. Rev. B* 85, 214105.
- Dorogokupets, P.I., Dewaele, A., 2007. Equations of state of MgO, Au, Pt, NaCl-B1, and NaCl-B2: internally consistent high-temperature pressure scales. *High Pressure Res.* 27, 431–446.
- Eremets, M.I., Trojan, I.A., 2009. Evidence of maximum in the melting curve of hydrogen at megabar pressures. *JETP Lett.* 89, 174–179.
- Errandonea, D., 2013. High-pressure melting curves of the transition metals Cu, Ni, Pd, and Pt. *Phys. Rev. B* 87, 5.
- French, M., Mattsson, T.R., 2014. Thermoelectric transport properties of molybdenum from ab-initio simulations. *Phys. Rev. B* 90, 165113.
- Gomi, H., Ohta, K., Hirose, K., Labrosse, S., Caracas, R., Verstraete, M.J., Hernlund, J.W., 2013. The high conductivity of iron and thermal evolution of the Earth's core. *Phys. Earth Planet. Inter.* 224, 88–103.
- Goncharov, A.F., Crowhurst, J.C., Dewhurst, J.K., Sharma, S., Sanloup, C., Gregoryanz, E., Guignot, N., Mezouar, M., 2007. Thermal equation of state of cubic boron nitride: implications for a high-temperature pressure scale. *Phys. Rev. B* 75, 224114.
- Goncharov, A.F., Beck, P., Struzhkin, V.V., Haugen, B.D., Jacobsen, S.D., 2009a. Thermal conductivity of lower-mantle minerals. *Phys. Earth Planet. Inter.* 174, 24–32.
- Goncharov, A.F., Montoya, J.A., Subramanian, N., Struzhkin, V.V., Kolesnikov, A., Somayazulu, M., Hemley, R.J., 2009b. Laser heating in diamond anvil cells: developments in pulsed and continuous techniques. *J. Synchrotron Radiat.* 16, 769–772.
- Goncharov, A.F., Struzhkin, V.V., Montoya, J.A., Kharlamova, S., Kundargi, R., Siebert, J., Badro, J., Antonangeli, D., Ryerson, F.J., Mao, W., 2010. Effect of composition, structure, and spin state on the thermal conductivity of the Earth's lower mantle. *Phys. Earth Planet. Inter.* 180, 148–153.
- Goncharov, A.F., Dalton, D.A., McWilliams, R.S., Mahmood, M.F., 2012a. Development of ultrafast spectroscopic techniques to study rapid chemical and physical changes in materials under extreme pressure and temperature conditions. *MRS Proc.* 1405.
- Goncharov, A.F., Wong, M., Dalton, D.A., Ojwang, J.G.O., Struzhkin, V.V., Konopkova, Z., Lazor, P., 2012b. Thermal conductivity of argon at high pressures and high temperatures. *J. Appl. Phys.* 111.
- Goncharov, A.F., Lobanov, S.S., Tan, X., Hohensee, G.T., Cahill, D.G., Lin, J.-F., Thomas, S.-M., Okuchi, T., Tomioka, N., 2015. Experimental study of thermal conductivity at high pressures: implications for the deep Earth's interior. *Phys. Earth Planet. Inter.*
- Haynes, W.M., 2011. *CRC Handbook of Chemistry and Physics*, 91st Ed. National Institute of Standards and Technology, Boulder, CO.
- Hofmeister, A.M., 2006. Thermal diffusivity of garnets at high temperature. *Phys. Chem. Miner.* 33, 45–62.
- Holmes, N.C., Moriarty, J.A., Gathers, G.R., Nellis, W.J., 1989. The equation of state of platinum to 660 GPa (6.6 Mbar). *J. Appl. Phys.* 66, 2962–2967.
- Hsieh, W.-P., Chen, B., Li, J., Keblinski, P., Cahill, D.G., 2009. Pressure tuning of the thermal conductivity of the layered muscovite crystal. *Phys. Rev. B* 80, 180302.
- Huang, X., Gao, C., Li, M., He, C., Hao, A., Zhang, D., Yu, C., Wang, Y., Sang, C., Cui, X., Zou, G., 2007. Finite element analysis of resistivity measurement with four point probe in a diamond anvil cell. *J. Appl. Phys.* 101.
- Jin, K., Wu, Q., Geng, H.Y., Li, X.Z., Cai, L.C., Zhou, X.M., 2011. Pressure–volume–temperature equations of state of Au and Pt up to 300 GPa and 3000 K: internally consistent pressure scales. *High Pressure Res.* 31, 560–580.
- Johannsen, P.G., Reiß, G., Bohle, U., Magiera, J., Müller, R., Spiekermann, H., Holzapfel, W.B., 1997. Refractive index of the alkali halides. II. Effect of pressure on the refractive index of 11 alkali halides. *Phys. Rev. B* 55, 6865–6870.
- Kavner, A., Jeanloz, R., 1998. High-pressure melting curve of platinum. *J. Appl. Phys.* 83, 7553–7559.
- Konopkova, Z., Lazor, P., Goncharov, A.F., Struzhkin, V.V., 2011. Thermal conductivity of hcp iron at high pressure and temperature. *High Pressure Res.* 31.
- Li, X.Y., Jeanloz, R., 1990. Laboratory studies of the electrical-conductivity of silicate perovskites at high-pressures and temperatures. *J. Geophys. Res. Solid Earth Planets* 95, 5067–5078.
- Manga, M., Jeanloz, R., 1997. Thermal conductivity of corundum and periclase and implications for the lower mantle. *J. Geophys. Res. Solid Earth* 102, 2999–3008.
- Mao, H.K., Xu, J., Bell, P.M., 1986. Calibration of the ruby pressure gauge to 800 kbar under quasi-hydrostatic conditions. *J. Geophys. Res. Solid Earth Planets* 91, 4673–4676.
- McWilliams, R.S., Dalton, D.A., Konôpková, Z., Mahmood, M.F., Goncharov, A.F., 2015. Opacity and conductivity measurements in noble gases at conditions of planetary and stellar interiors. *Proc. Natl. Acad. Sci.* <http://dx.doi.org/10.1073/pnas.1421801112>.
- Montoya, J.A., Goncharov, A.F., 2012. Finite element calculations of the time dependent thermal fluxes in the laser-heated diamond anvil cell. *J. Appl. Phys.* 111, 9.
- Ohta, K., Yagi, T., Taketoshi, N., Hirose, K., Komabayashi, T., Baba, T., Ohishi, Y., Hernlund, J., 2012. Lattice thermal conductivity of MgSiO₃ perovskite and post-perovskite at the core-mantle boundary. *Earth Planet. Sci. Lett.* 349, 109–115.
- Okada, T., Itaka, T., Yagi, T., Aoki, K., 2014. Electrical conductivity of ice VII. *Sci. Rep.* 4, 5.
- Olson, P., 2013. The new core paradox. *Science* 342, 431–432.
- Parker, W.J., Jenkins, R.J., Abbott, G.L., Butler, C.P., 1961. Flash method of determining thermal diffusivity, heat capacity, and thermal conductivity. *J. Appl. Phys.* 32, 1679.
- Pozzo, M., Davies, C., Gubbins, D., Alfe, D., 2012. Thermal and electrical conductivity of iron at Earth's core conditions. *Nature* 485, U355–U399.
- Seagle, C.T., Cottrell, E., Fei, Y.W., Hummer, D.R., Prakapenka, V.B., 2013. Electrical and thermal transport properties of iron and iron-silicon alloy at high pressure. *Geophys. Res. Lett.* 40, 5377–5381.

- Shimizu, K., Kimura, T., Furomoto, S., Takeda, K., Kontani, K., Onuki, Y., Amaya, K., 2001. Superconductivity in the nonmagnetic state of iron under pressure. *Nature* 412, 316–318.
- Slack, G.A., 1964. Platinum as a thermal conductivity standard. *J. Appl. Phys.* 35, 339.
- Stacey, F.D., 1992. *Physics of the Earth*, 3rd Ed.
- Stacey, F.D., Anderson, O.L., 2001. Electrical and thermal conductivities of Fe–Ni–Si alloy under core conditions. *Phys. Earth Planet. Inter.* 124, 153–162.
- Stacey, F.D., Loper, D.E., 2007. A revised estimate of the conductivity of iron alloy at high pressure and implications for the core energy balance. *Phys. Earth Planet. Inter.* 161, 13–18.
- Vlček, V., de Koker, N., Steinle-Neumann, G., 2012. Electrical and thermal conductivity of Al liquid at high pressures and temperatures from ab initio computations. *Phys. Rev. B* 85, 7.
- Wilthan, B., Cagran, C., Brunner, C., Pottlacher, G., 2004. Thermophysical properties of solid and liquid platinum. *Thermochim. Acta* 415, 47–54.
- Yagi, T., Ohta, K., Kobayashi, K., Taketoshi, N., Hirose, K., Baba, T., 2011. Thermal diffusivity measurement in a diamond anvil cell using a light pulse thermoreflectance technique. *Meas. Sci. Technol.* 22, 024011.
- Zhang, P., Cohen, R.E., Haule, K., 2015. Effects of electron correlations on transport properties of iron at Earth's core conditions. *Nature* 517, 605–607.